Electronic Supplementary Material (ESI) for Materials Advances.
This journal is © The Royal Society of Chemistry 2022

Supplementary material

Ultraflexible All-in-one Supercapacitors with High Capacitance and Ultrastable Cycle Performance Enabled by Wood Cellulose Network

Shaoqiu Ke[a,b,1], Di Xie[b,1],Kai Zhang[b], Fangchao Cheng[a,b,*], Yiqiang Wu[a,*]

[a] College of Material Science and Engineering, Central South University of Forestry and Technology, Changsha 410004, China

[b] Guangxi Key Laboratory of Processing for Nonferrous Metallic and Featured Materials, School of Resources, Environment and Materials, Guangxi University, Nanning 530004, China

[1]These authors made equal contributions to this paper.

*Corresponding authors: fangchaocheng@gxu.edu.cn; wuyq0506@126.com

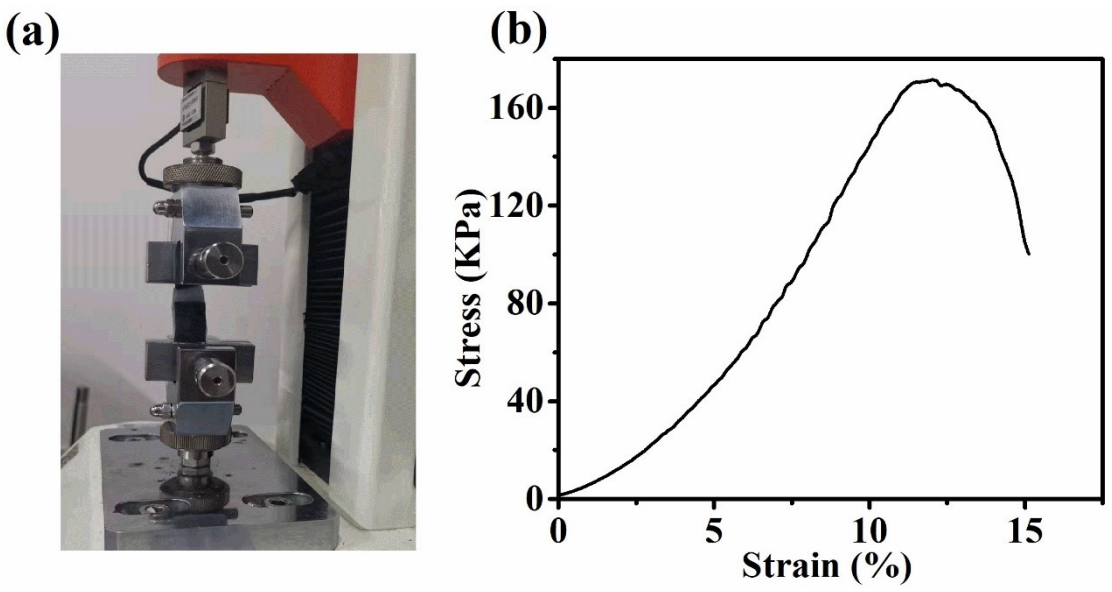

Fig. S1 (a) The tensile test of the all-in-one supercapacitor, (b) the typical stress-strain curve.

24 *Fourier-transform infrared (FTIR) analysis.* FTIR spectra of multiwalled carbon
25 nanotube (MWCNT), polyaniline (PANI), cellulose network, and cellulose
26 network/polyaniline/multiwalled carbon nanotube (CPM) samples were compared to
27 analyze the interaction among PANI, MWCNT, and the cellulose network in the
28 composites. In the cellulose network spectrum (Fig. Sla), the characteristic peak at
29 3426 cm^{-1} was assigned to -OH stretching [1], and the absorption peaks at 2920, 1639,
30 1428, and 1062 cm^{-1} were assigned to C-H stretching, conjugated C=O stretching, -
31 CH_2 and -OCH- plane bending, and C-O-C stretching, respectively [2]. The
32 fractionation process removed most hemicellulose and lignin fractions while leaving
33 the cellulose network intact [2], and the characteristic peaks of cellulose dominated the
34 purified wood spectrum. The comparison of the FTIR spectra of wood and the
35 cellulose network (Fig. S2a) also confirmed the above inference. The disappearance
36 of the characteristic peak of aromatic skeleton vibration in lignin at 1505 cm^{-1} and the
37 characteristic peak of the acetyl group in hemicellulose at 1739 cm^{-1} indicated that
38 lignin and hemicellulose were removed after the fractionation process [3]. In the
39 spectrum of PANI (Fig. 2i), the peaks at 1558, 1479, 1297, and 796 cm^{-1} were
40 assigned to the C=C stretching deformation of quinoid rings, C=C stretching
41 deformation of benzenoid rings [4], C-N stretching band of an aromatic amine, and out-
42 of-plane deformation of C–H in the 1,4-disubstituted benzene ring of PANI,
43 respectively [5]. In particular, the intensity of the absorption peak at 1479 cm^{-1} was
44 greater than that at 1558 cm^{-1}, indicating that there were more benzene rings than

quinones in the PANI molecular chains [5]. Additionally, the FTIR spectrum of the CPM composite (Fig. 2i) confirmed the interaction between the cellulose network and PANI during the formation of the composite [6]. The intensity of the peak at 3400 cm^{-1} for the CPM composites was significantly reduced in comparison to that of the cellulose network spectrum, possibly ascribed to the influence of PANI particles on the hydrogen bonds in cellulose [6]. This suggested an increase in the electron density of PANI, which can result in an increase of the conductivity [5]. The characteristic peaks for C=C stretching vibrations in the quinone and benzene rings at 1530 and 1493 cm^{-1} were also observed in the spectrum of CPM composites with varied intensities compared to that of the PANI. The FTIR spectrum of CPM showed high similarity to those of MWCNT, PANI, and the cellulose network, which confirmed that the MWCNT and PANI layers were successfully infiltrated into the cellulose network.

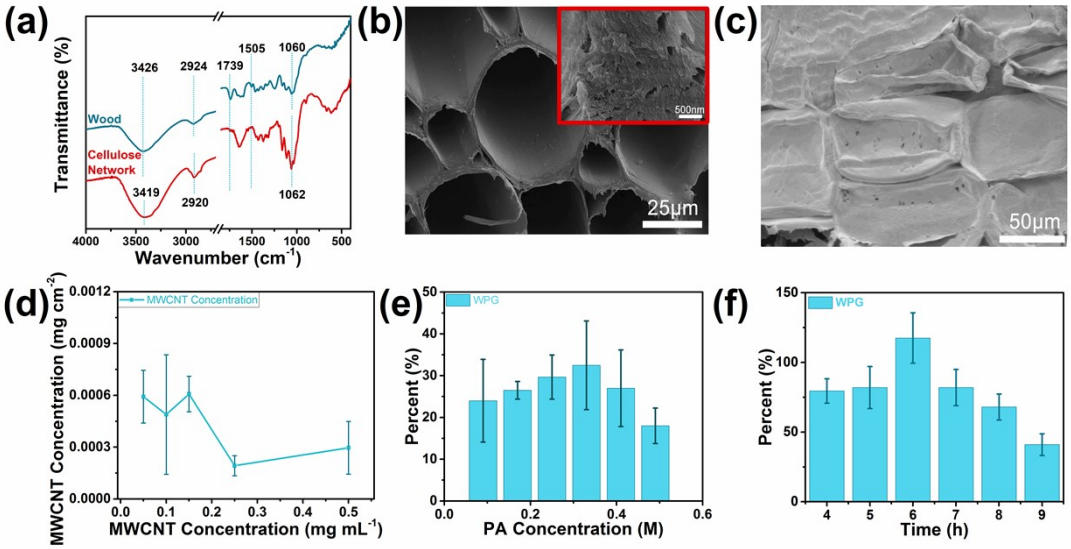

Fig. S2 (a) FTIR spectra of the wood and cellulose network samples, (b) SEM images for the cross-section of the cellulose network, (c) SEM images for the longitudinal section of the cellulose network, (d) the effect of MWCNT concentration on the MWCNT loading in the cellulose network, (e) WPG of the CPM composites prepared with different PA concentrations, and (f) WPG of the CPM composites prepared with different reaction time.

Microstructure of the cellulose network. Fig. S2 also presents the microstructure of the cellulose network after the removal of hemicellulose and lignin. It can be clearly seen that the microfibril structure of wood was exposed after the fractionation process (Fig. S2b). Meanwhile, the pit structure on the cell wall of wood was also destroyed, resulting in the passage between the adjacent wood cells (Fig. S2c).

Optimization of the preparation process of the CPM composites. Fig. S2d illustrates the effect of MWCNT concentration on the MWCNT loading in the cellulose network when immersing aqueous MWCNT solution into the cellulose network. The MWCNT concentration showed limited influence of the loading when the concentration ranged from 0.05 to 0.15 mg mL^{-1}, and the higher concentration led

78 to lower MWCNT loading. A MWCNT concentration of 0.15 mg mL^{-1} was selected
79 to conduct the immersion process in this study. Fig. S2e-f summarizes the weight
80 percent gain (WPG) results of the cellulose network during the *in situ* polymerization
81 process. The PA concentration and polymerization time exhibited an important
82 influence on the WPG, and the optimized conditions (0.33 M and 6 h) were chosen to
83 prepare the CPM composites.

84 *Raman analysis.* Raman spectra of MWCNT and CPM samples were compared
85 to investigate the effect of the preparation process on the structure of MWCNT (Fig.
86 2j). The Raman spectra revealed the featured D, G, and D* bands for MWCNT at
87 1346, 1580, and 2689 cm^{-1}, respectively [7], and these three bands appeared at 1389,
88 1572, and 2803 cm^{-1}, respectively, in the spectra of the CPM composites. The high
89 similarity between the Raman spectra of CPM and MWCNT indicated the limited
90 effect of the process on the structure of MWCNT.

91 *X-ray-diffraction (XRD) analysis.* The XRD patterns of MWCNT, PANI, the
92 cellulose network, and CPM samples (Fig. 2k) were compared to investigate the
93 potential change of crystal structure during the preparation process of CPM
94 composites. Three broad peaks at 2θ = 15.9°, 20.6°, and 25.4° were revealed in the
95 XRD pattern of PANI, which corresponded to the (010), (100), and (110) planes,
96 respectively [8]. Among these peaks, the two peaks at 2θ = 15.9° and 20.6° were
97 attributed to periodicity parallel to the polymer chains, and the peak at 2θ = 25.4° was
98 attributed to periodicity perpendicular to the polymer chains. As previously reported [9],

PANI was mainly a non-crystalline substance, which was consistent with the results in this study. The XRD pattern of the cellulose network sample showed three peaks at 2θ = 15.9°, 22.6°, and 35.0°, which were attributed to the diffraction of the (010), (002), and (040) planes of cellulose, respectively [2]. The XRD pattern of the MWCNT sample showed two typical peaks at 2θ = 26.0° and 43.1°, which were attributed to the diffraction of the (002) and (100) planes, respectively [10], indicating the crystallinity of MWCNT. The XRD pattern of the CPM sample showed a similarity with those of PANI, MWCNT, and the cellulose network with the reduced intensity of peaks attributed to cellulose, indicating the partial destruction of the crystalline structure of cellulose. The relative crystallinity of cellulose decreased from 60.23% for cellulose network samples to 54.97% for CPM composites. This may be attributed to the non-crystalline nature of PANI [9], which can partially break the intermolecular hydrogen bonding in cellulose and decrease the cellulose crystallinity of cellulose network samples during the *in situ* polymerization of aniline monomers [11].

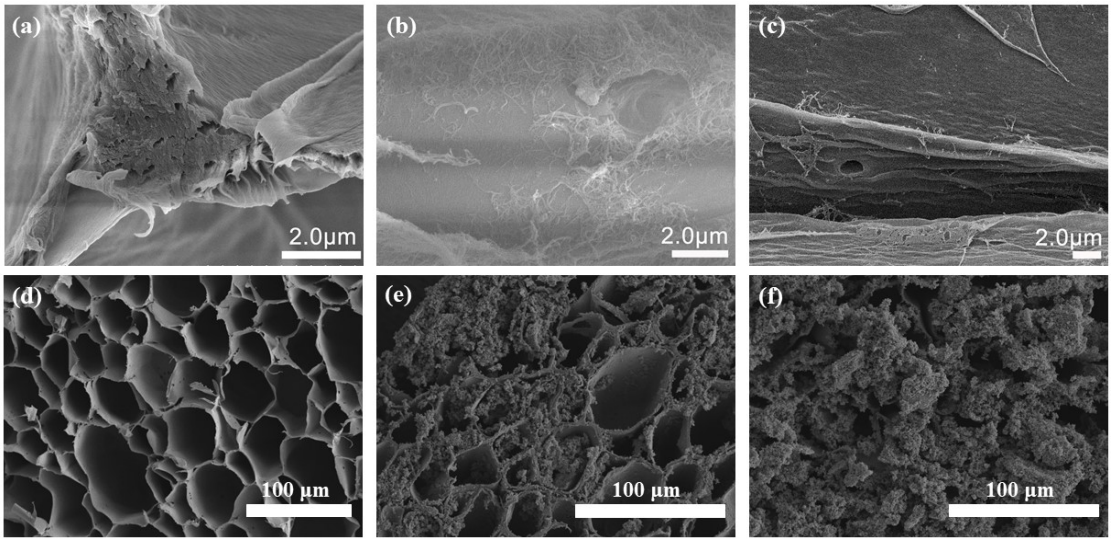

Fig. S3 (a-c) SEM image of the distribution of MWCNT from the surface to the center, (d) SEM image of CPM loaded with 0 mg cm^{-2} MWCNT, (e) SEM of CPM loaded with 3.6 mg cm^{-2} MWCNT, (f) SEM of CPM loaded with 7.2 mg cm^{-2} MWCNT.

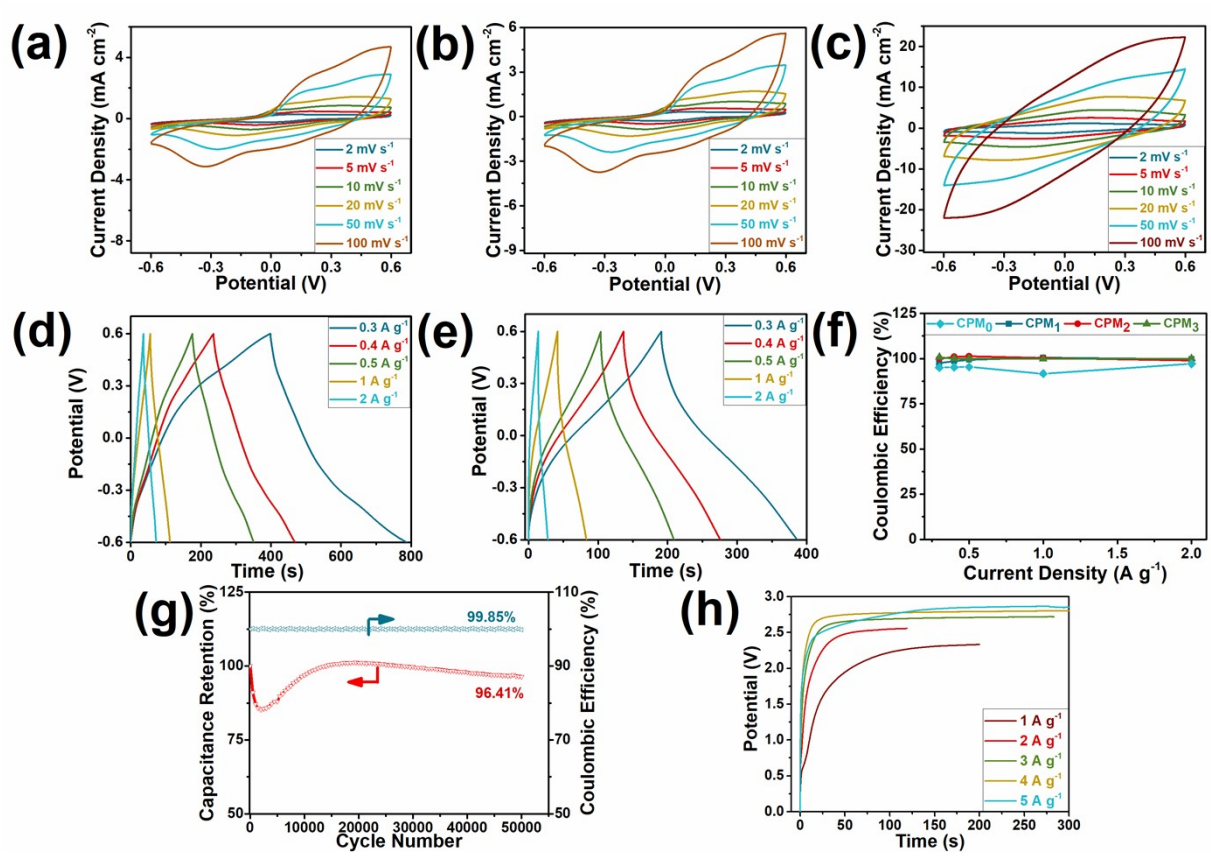

Fig. S4 Electrochemical performance of the integrated FSCs based on the single CPM blocks with MWCNT of various weights: CV curves for (a) CPM_0, (b) CPM_1, and (c) CPM_2 based FSCs under various sweep rates; GCD curves for (d) CPM_1 and (e) CPM_2 based FSCs under various current densities; (f) Coulombic efficiency of the CPM_X-based FSCs under various current densities; (g) capacitance retention and Coulombic efficiency of the CPM_2-based FSC in the cyclic charge and discharge test at 5 A g^{-1}; (h) maximum charging voltage of the CPM_2-based FSC at various current densities after 50000 cycles at 3 A g^{-1}.

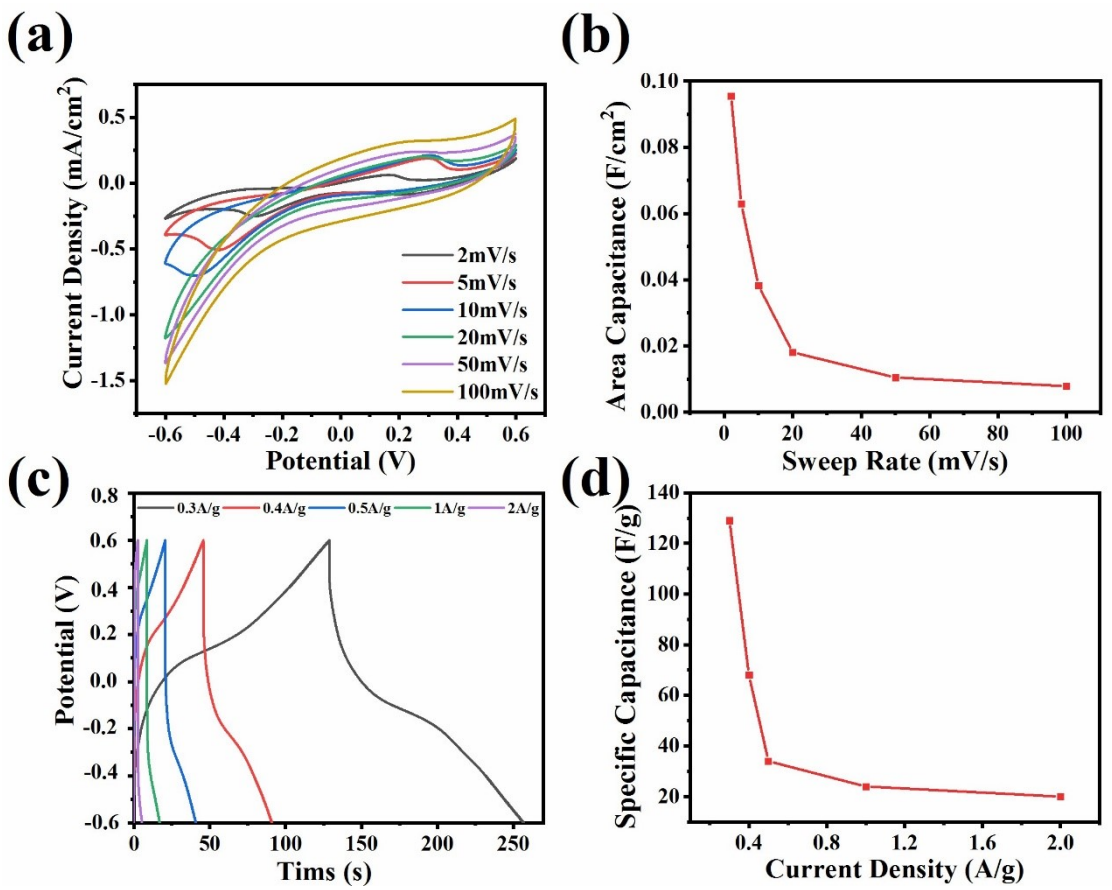

Fig. S5 (a) CV curves, (b) areal specific capacitance, (c) GCD curves, and (d) gravimetric specific capacitance for the comparison CPM samples prepared by dipping the electrolyte and subsequently applying MWCNT and PANI.

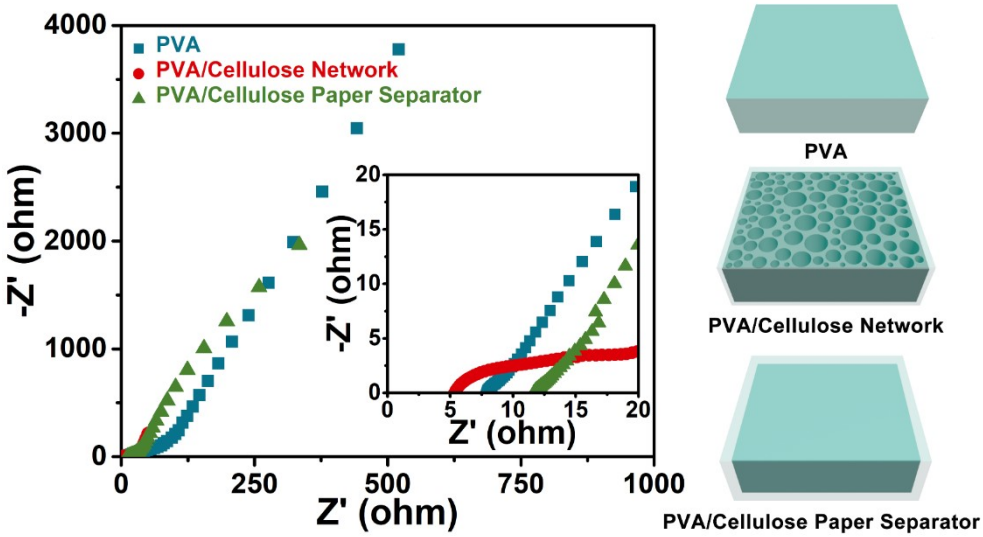

Fig. S6 Nyquist diagrams for PVA, PVA/cellulose network, and PVA/cellulose paper separator.

References

1. A. Mandal and D. Chakrabarty, *Carbohydr. Polym.*, 2011, **86**, 1291-1299.
2. H. J. Marrinan and J. Mann, *J. Polym. Sci.*, 1956, **21**, 301-311.
3. N. Sun, M. Rahman, Y. Qin, M. L. Maxim, H. Rodríguez and R. D. Rogers, *Green. Chem.*, 2009, **11**, 646-655.
4. W. L. Hu, S. Y. Chen, Z. H. Yang, L. T. Liu and H. P. Wang, *J. Phys. Chem. B*, 2011, **115**, 8453-8457.
5. W. He, J. P. Li, J. X. Tian, H. Jing and Y. J. Li, *Polym. Compos.*, 2018, **39**, 537-543.
6. D. Xu, X. Xiao, J. Cai, J. Zhou and L. Zhang, *J Mater Chem A*, 2015, **3**, 16424-16429.
7. H. Wang, C. Wang, M. Jian, Q. Wang, K. Xia, Z. Yin, M. Zhang, X. Liang and Y. Zhang, *Nano. Res.*, 2018, **11**, 2347-2356.
8. Y. T. Ravikiran, S. Kotresh, S. C. Vijayakumari and S. Thomas, *Curr. Appl. Phys.*, 2014, **14**, 960-964.
9. J. Lin, G.-J. Zhao, L.-X. Meng and Z.-P. Li, *SPECTROSC SPECT ANAL*, 2010, **30**, 1674-1677.
10. J. D. Kim, H. Yun, G. C. Kim, C. W. Lee and H. C. Choi, *Appl. Surf. Sci.*, 2013, **283**, 227-233.
11. B. Anothumakkool, R. Soni, S. N. Bhange and S. Kurungot, *Energ Environ Sci*, 2015, **8**, 1339-1347.